

## Article

# Viability of Bauxite Deposits from Catalonia (Spain) for Ceramic Applications

Arnau Martínez <sup>1</sup>, Maite Garcia-Valles <sup>2</sup>  and Pura Alfonso <sup>1,\*</sup> 

<sup>1</sup> Departament d'Enginyeria Minera, Industrial i TIC, Universitat Politècnica de Catalunya Barcelona Tech, Av. Bases de Manresa 61-63, 08242 Manresa, Spain

<sup>2</sup> Departament de Mineralogia, Petrologia i Geologia Aplicada, Universitat de Barcelona, Carrer Martí i Franquès, s/n, 08028 Barcelona, Spain; maitegarciavalles@ub.edu

\* Correspondence: maria.pura.alfonso@upc.edu

**Abstract:** This study provides a characterization of materials from wastes and outcrops of two inactive bauxite mines located close to Sant Joan de Mediona and Peramola, Spain. Mineralogy was determined via powder X-ray diffraction (XRD) and Fourier transform infrared spectroscopy (FTIR). Thermal properties were measured via differential thermal analysis–thermogravimetry (DTA-TG) and gresification tests. The crystalline phases are medium-high crystalline kaolinite and variable amounts of illite, quartz, calcite, boehmite, hematite and rutile/anatase. DTA show two endothermic peaks produced by the dehydroxylation of minerals: the first peak, at 530–538 °C, belongs to boehmite; the second peak, at 535–568 °C, corresponds to kaolinite. An exothermic peak at 950–978 °C is associated with mullite crystallization. The optimal sintering temperatures obtained from the gresification curves (firing shrinkage and water absorption) were 970 °C for carbonate-poor, illite-rich clays; 1100 °C for illite- and carbonate-poor samples; and near 1190 °C for carbonate-rich materials. The carbonate-poor samples fired at 1300 °C contain sillimanite and mullite, and the carbonate-rich materials are rich in gehlenite, anorthite, and hedenbergite. The mineralogy of these materials is sufficient to obtain ceramic materials with suitable properties, but not their low plasticity. They could be used in the formulation of bricks or as part of mixtures to produce refractory ceramics.

**Keywords:** bauxite; kaolinite; mineralogy; firing; shrinkage; water absorption; gresification



**Citation:** Martínez, A.; Garcia-Valles, M.; Alfonso, P. Viability of Bauxite Deposits from Catalonia (Spain) for Ceramic Applications. *Minerals* **2023**, *13*, 1294. <https://doi.org/10.3390/min13101294>

Academic Editor: Felix Brandt

Received: 5 September 2023

Revised: 29 September 2023

Accepted: 2 October 2023

Published: 4 October 2023



**Copyright:** © 2023 by the authors. Licensee MDPI, Basel, Switzerland. This article is an open access article distributed under the terms and conditions of the Creative Commons Attribution (CC BY) license (<https://creativecommons.org/licenses/by/4.0/>).

## 1. Introduction

The applications of kaolin are increasing day by day. In addition to the traditional uses [1], there are new applications; for example, as a raw material in the manufacture of alternative materials to Portland cement in order to reduce the gas emissions produced during its manufacture [2–4]. As a result, demand for kaolin is increasing significantly, although its availability is decreasing [5]. Therefore, it is essential to find new sources of kaolin supply. One such source is bauxite deposits, which usually contain significant amounts of kaolin. Both bauxite mining tailings and waste from bauxite processing and metallurgy are being explored as a source of kaolin [6,7]. Extensive research has already been carried out for both the application of bauxite waste as a cementitious material [2] and its use as a ceramic raw material [8–10].

In addition, the use of mining wastes has great environmental advantages. On the one hand, these wastes are removed from the environment, where they can produce different types of impacts; on the other hand, this reduces the volume of materials that must be extracted from their natural position and thus reduces the energy required for extraction and the formation of new wastes.

Spain ranked first in Europe for kaolin imports in 2020 [5]. Although there are some important deposits of kaolin in Spain, they mainly occur in Galicia, with important deposits produced via the kaolinization of Variscan granitic rocks [11], and in the Teruel and Valencia regions, where they are secondary deposits located in the Utrillas Formation, Lower

Cretaceous age [12]. The supply chain of ceramic raw materials in Spain is moderately dependent on relatively distant countries, mainly Ukraine [13]. This carries a high risk of supply risk, as evidenced by the war in Ukraine. In addition, from an environmental point of view, the transport of raw materials that are needed in large quantities, as well as making the product more expensive, entails energy costs that result in gas emissions into the atmosphere.

In Catalonia, the need for kaolin is greater than its current availability. In the north-east of Spain, multiple occurrences of bauxitic materials have been reported [14–18]. The size of these deposits is generally small, although some of them were mined in the past, leaving a large accumulation of wastes in their surroundings, as in the case of the la Llacuna, Peramola, and Purisima mines. This last is located in the southernmost part of Catalonia, and it is known as a bauxite mine, although detailed studies have demonstrated that it is a kaolinitic clay deposit [19]. In no cases were these bauxitic materials used for the manufacture of ceramics, nor are there any studies that show their suitability for this application. This paper characterizes materials from two of the most important bauxite deposits in Catalonia, northeast Spain, in order to determine their viability for use as ceramic raw materials. The old bauxite mining wastes studied are localized near the localities of Peramola and Sant Joan de Mediona. Both were exploited until the 20th century.

## 2. Materials and Methods

### 2.1. Study Area

The bauxitic materials studied here come from two areas in Catalonia, NE Spain, which were mined in the past. One of them is the wastes and materials from the Esperanza mine from Peramola, which is located in the Pre-Pyrenean range. The other materials are close to Sant Joan de Mediona in the prelitoral range; both are located at the border of these units with the Ebro depression (Figure 1).

The bauxites of Peramola are located in the south-central unit of the Pyrenees. This unit is divided, from north to south, into the Boixols, Montsec, and Sierras Marginales sub-units [20], these being bauxites in the Sierras Marginales sub-unit, which are composed of Mesozoic rocks overlain by Tertiary detrital rocks. The materials in the area correspond to Liassic limestone, followed by massive Dogger dolomites and Malm limestone and marls. They are covered by Upper Cretaceous rocks, which are in tectonic contact with Igualada marls of Bartonian age, middle Eocene, which are found in the core of the Oliana anticline [21]. In the study area, these materials are covered by Upper Eocene detrital ochre-colored sandstones and clays from the Priabonian, which grade towards the west to coarser materials, with conglomerates coming to the surface.

The bauxite deposits are hosted in the Liassic limestones, close to the border with the SW end of the Oliana anticline, of NNE–SSW orientation, and constituted by Eocene materials. This specific boundary corresponds to the Segre thrust, which delimits the south-central unit of the Pyrenees with the Ebro depression [21]. At this site, the thickness of the bauxite layers is variable, i.e., from a few cm to 10 m.

The bauxites of Sant Joan de Mediona are located in the Prelitoral range. This is an area with abundant evidence of bauxites, including those of La Llacuna, Santa Maria de Miralles, and Sant Quintí de Mediona. The bauxites are found in karstic pockets within Mesozoic carbonate materials, which, in some cases, correspond to the Lower Muschelkalk, and in others, to the Upper Muschelkalk [14,22], and even in the Keuper units [23,24], such as the Sant Joan de Mediona (Figure 1).

In the outcrops, the bauxitic materials present the typical reddish, pinkish, and even almost-white pisolitic aspect, which are found mixed in the same outcrop.

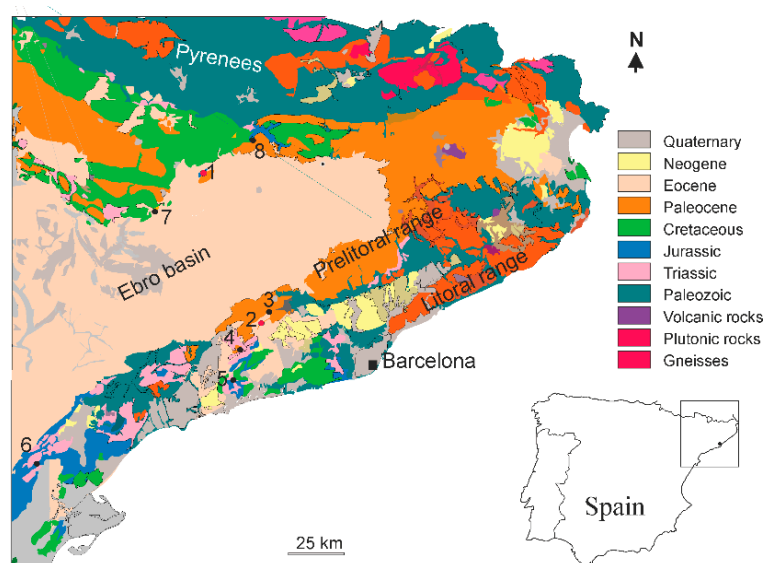


**Figure 1.** Geological map of Catalonia with the location of the two study areas (red dots 1 and 2), as well as other previously reported bauxite deposits from Catalonia: 3–5 [18]; 6 [19]; 7 [22]; 8 [24].

## 2.2. Sampling

In both Peramola and Sant Joan de Mediona, representative samples were taken from dumps, outcrops, and inside the ancient mine shafts. A total of 17 samples were taken in Peramola (P), and 5 samples in Sant Joan de Mediona (JM). Some samples were cohesioned rocks, while others consisted of earthy material. In the first case, they were crushed and ground. All of them were then sieved and split to obtain the amount of sample required to perform the chemical and mineralogical analyses. Once these results were obtained, those samples that gave very similar results were mixed. Finally, the gresification tests were carried out with three samples, which represent more than 80% of the materials from each of the two areas.

## 2.3. Analytical Methods

The chemical composition of major elements was obtained via inductive coupled analysis in the ALS Global laboratories. Additional chemical analyses have been carried out using a portable X-ray Fluorescence (XRF) with Epsilon 1 equipment from the PANalytical company/Malvern, United Kingdom. The major elements analyzed were Si, Al, Ti, Fe, Mn, Mg, Ca, Na, K, and P.

Mineralogy of raw materials and fired ceramics was determined via powder X-ray diffraction (XRD) using non-oriented and oriented aggregates. XRD measurements were taken using an automatic X'Pert PANalytical diffractometer with graphite monochromator, automatic gap,  $K\alpha$ -radiation of Cu at  $\lambda = 1.54061 \text{ \AA}$ , powered at 45 kV and 40 mA, with a scanning range of  $4\text{--}100^\circ$  with a  $0.017^\circ$   $2\theta$  step scan, and a 50 s measuring time. In addition, oriented aggregates of the samples were prepared following the standard XRD procedures [25]. The XRD patterns were obtained for oriented samples after the following pre-treatments: air drying at room temperature, saturation with ethylene glycol, and after-heating at  $550^\circ\text{C}$  for 1 h. Identification and semi-quantitative evaluation of phases were made on PANalytical X'Pert HighScore software, Version 2.0.1. (PANalytical, Almelo, The Netherlands). Calculation of the Hinckley crystallinity index of kaolinite was obtained according to [26]. The crystallite size of kaolinite was determined using the Scherrer equation.

Fourier transform infrared (FTIR) and scanning electron microscopy (SEM) completed the characterization. FTIR spectra were obtained in powder using a 2000 FTIR Perkin–Elmer spectrometer, Waltham, MA, USA. Vibrational spectra were obtained in the  $400\text{--}4000 \text{ cm}^{-1}$  range.

Back-scattered electron images of the kaolinitic raw and treated materials were obtained using a Hitachi TM-1000 table-top SEM (High-Technologies Corporation, Tokyo, Japan) equipped with an energy dispersive X-ray spectrometer (EDS).

The Atterberg limits were calculated to determine the plasticity indices of these materials: the liquid limit (LL) from the Spanish standard UNE 7-377-75 [27] versus the plasticity index (PI) from the standard UNE 103-104-93 [28]. The PI is the difference between the LL and the plastic limit (PL), which was obtained using the Casagrande apparatus following the method described in the Spanish standard.

Thermal analyses of raw materials were obtained via simultaneous differential thermal analysis and thermogravimetry (DTA–TG), using a TASCHE 414/3 model (Netzsch, Selb, Germany). Analyses were carried out in the range 25–1300 °C under air atmosphere at a constant flow rate of 80 mL min<sup>−1</sup> in an alumina crucible and at a heating rate of 10 °C min<sup>−1</sup>. The amount of sample used was 85 mg.

#### 2.4. Technological Tests

The viability of the bauxite materials studied for ceramic applications was determined from the gresification curves. These consist of the representation of linear firing shrinkage and water absorption versus temperature in the same plot and are extensively used [29,30]. The intersection of both curves indicates the optimum firing temperature of the raw material to manufacture ceramics.

Nine tests pieces from each sample have been prepared to determine the water absorption and linear shrinkage. The test pieces were made by mixing 60-g samples with water and placing them in 4 × 3 × 6 mm molds. After compaction, the sample excess was cut off using a spatula and marked with a 3-cm-long mark to measure the linear shrinkage after firing. The resulting pieces were air-dried and then oven-dried to 105 °C until a constant weight. The pieces were sintered in an electric furnace at 900, 1000, 1050, 1100, 1150, 1175, 1200, 1250, and 1300 °C. The heating rate was 2 °C min<sup>−1</sup>, with a holding time of 120 min at the end of the heating. After heating, the length of the previously made mark was measured to determine the linear shrinkage of the tiles. To determine the water absorption, the tiles were weighted. Then, they were placed in a vertical position inside a recipient, covering up to one third of their height with water, and left for 30 min. Then, the recipient was filled up to the total height of the tiles, closing the recipient and boiling the water for 2 h. Finally, the fire was turned off, and the tiles were left to cool for 4 h, after which the tiles were removed, and the excess moisture was dried with a damp cloth and weighed, obtaining the mass of water absorbed.

The color parameters were measured in the raw materials and in the fired samples using a CM-700d Konica-Minolta spectrophotometer over the visible range [31]. Color can be described through parameters L\*, a\*, and b\*, where L\* = 100 is white and L\* = 0 is black; a\* > 0 is red and a\* < 0 is green; b\* > 0 is yellow and b\* < 0 is blue [32].

### 3. Results

#### 3.1. Chemical Composition

The chemical compositions of kaolinitic raw materials from Peramola and Sant Joan de Mediona are presented in Table 1. The content of the major elements is highly variable. SiO<sub>2</sub> content ranges from 7.91 to 48 wt%; Al<sub>2</sub>O<sub>3</sub> is between 10.42 and 59.67 wt%; Fe<sub>2</sub>O<sub>3</sub> ranges from 8.44 to 27.70 wt%; CaO can reach up to 24.52% wt%; and TiO<sub>2</sub> is between 1.14 and 3.98 wt%. Alkali contents are low, with Na<sub>2</sub>O ranging from 0.04 to 0.20 wt%; and K<sub>2</sub>O is between 0.02 and 3.14 wt% (Table 1).

**Table 1.** Chemical composition (wt%) of several samples from Peramola (P) and Sant Joan de Mediona (JM) to show the high diversity of composition between both areas.

Sample	SiO <sub>2</sub>	Al <sub>2</sub> O <sub>3</sub>	TiO <sub>2</sub>	Fe <sub>2</sub> O <sub>3</sub>	MnO	MgO	CaO	Na <sub>2</sub> O	K <sub>2</sub> O	P <sub>2</sub> O <sub>5</sub>	LOI	SiO <sub>2</sub> /Al <sub>2</sub> O <sub>3</sub>	Al <sub>2</sub> O <sub>3</sub> /Fe <sub>2</sub> O <sub>3</sub>
P1	9.51	47.20	2.16	27.70	0.00	0.07	0.15	0.04	0.02	0.05	12.40	0.20	2.08
P2	48.0	27.10	1.14	8.44	0.00	0.64	0.32	0.20	1.99	0.06	11.85	1.77	3.21
P3	30.50	34.60	1.71	19.40	0.01	0.10	0.32	0.04	0.10	0.02	12.95	0.88	1.78
P10-B	18.58	42.97	2.91	1.35	0.00	0.00	0.29	-	0.04	0.36	-	0.43	31.8
P11-A	25.29	28.74	1.75	21.60	0.00	0.00	0.89	-	2.62	0.00	-	0.88	1.33
P11-B	47.03	12.66	0.82	5.85	0.02	0.73	8.69	-	2.88	0.42	20.93	2.16	0.67
P14-1	14.73	29.62	1.98	28.07	0.02	0.00	9.42	-	0.17	0.00	-	0.50	1.06
P14-3	35.39	29.21	1.53	12.81	0.02	0.01	0.32	-	2.94	-	-	0.87	2.28
P15-1	8.97	32.15	2.08	38.40	0.00	0.00	0.64	-	0.05	0.38	-	0.28	0.84
P15-4	16.75	41.64	2.65	24.80	0.00	0.00	4.76	-	0.23	0.42	-	1.68	5.21
JM 1	24.00	42.80	2.39	18.00	0.01	0.10	0.16	0.05	0.02	0.06	12.85	0.56	2.38
JM 2	23.43	16.69	0.95	8.21	0.01	0.43	24.52	0.06	0.60	0.08	25.02	1.40	2.03

-: not analyzed.

The Al<sub>2</sub>O<sub>3</sub>/Fe<sub>2</sub>O<sub>3</sub> ratio is used to determine the applicability of clays. If this is >5.5 alumina-rich clays, then they are useful for manufacturing refractory ceramics. If Al<sub>2</sub>O<sub>3</sub>/Fe<sub>2</sub>O<sub>3</sub> < 5.5, iron-rich clays can be used in the manufacture of bricks, tiles, and yellow-gray tableware [19]. In all samples, Al<sub>2</sub>O<sub>3</sub>/Fe<sub>2</sub>O<sub>3</sub> is lower than 5.5, except for one sample. The SiO<sub>2</sub>/Al<sub>2</sub>O<sub>3</sub> ratio also shows low values, i.e., between 0.20 and 1.77. Their reduced alkali contents suggest a high firing temperature when used in the formulation of the composition of a ceramic paste [19].

According to the Fe<sub>2</sub>O<sub>3</sub>-Al<sub>2</sub>O<sub>3</sub> + TiO<sub>2</sub>-SiO<sub>2</sub> ternary diagram [33] the San Joan de Mediona materials are clayey bauxites, whereas those from the Peramola plot also in the bauxitic clay (Figure 2). The chemical composition of these materials is similar to other bauxitic materials reported from Catalonia [18,19,23,24]. Part of the samples obtained in the present study in Peramola correspond to more clayey zones, plotting into the field of bauxitic clays, which is an aspect of interest from the point of view of their use in the manufacture of ceramics.

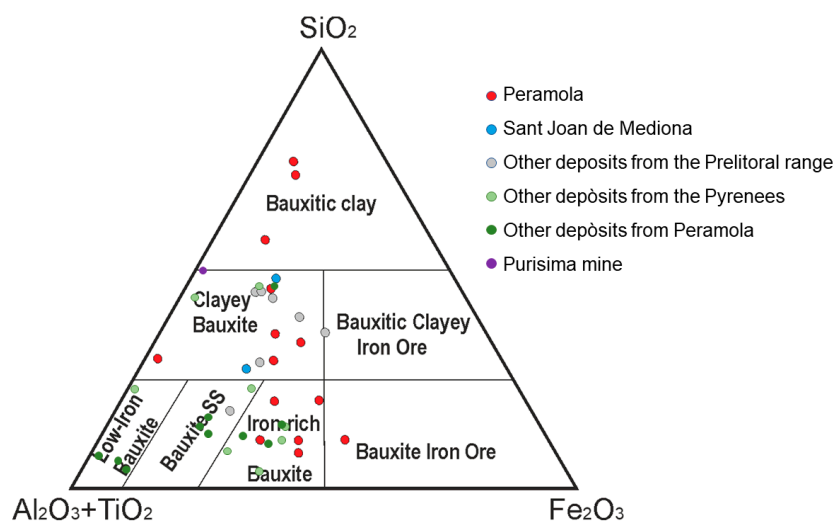


**Figure 2.** Classification of the Peramola and Sant Joan de Mediona materials on the Fe<sub>2</sub>O<sub>3</sub>-SiO<sub>2</sub>-Al<sub>2</sub>O<sub>3</sub> + TiO<sub>2</sub> ternary diagram [33], and comparison with other bauxitic materials from Catalonia: Prelitoral range [18], Pyrenees [23], Peramola [24] and Purisima mine [19].

### 3.2. Mineralogical Composition

The mineralogy of the studied samples is summarized in Table 2. Kaolinite is the main clay mineral, accounting for up to 68% by weight in Peramola and 60% in Sant Joan de Mediona. Boehmite can reach up to 54 wt%. The hematite content ranges from 1 wt% to 17 wt% by weight; rutile and anatase are also present around 1%–3% by weight. Calcite is variable, from <1 wt% to 54 wt%. Only in two cases was illite found. These results show

similar mineralogical compositions to other bauxite areas of NE Spain [18,34]. Therefore, the results of the present research are applicable to other areas of Catalonia.

To confirm the clay mineral type, oriented aggregates were prepared and analyzed via XRD (Figure 3). It was determined that in most cases, the clay mineral phase is kaolinite, and illite can only locally occur.

**Table 2.** Mineralogical composition (wt%) and HI of samples representative of the diversity of composition from Peramola (P) and Sant Joan de Mediona (JM).

Sample	Kaolinite	Quartz	Bohemite	Hematite	Goethite	Rutile/Anatase	Calcite	Illite	Zircon	HI
P 1	28	-	54	15	-	3	-	-	-	1.39
P 2	43	28	-	3	-	2	-	24	-	0.51
P 3	68	-	16	13	-	2	-	-	-	0.96
P 10-B	47	-	51	-	-	2	-	-	-	1.12
P 11-A	60	-	13	15	4	4	4	-	4	0.95
P 11-B	5	45	-	1	-	1	9	39	-	-
P 14-1	30	-	32	16	-	2	20	-	-	1.06
P14-3	49	9	1	4	5	2	-	29	-	1.22
P 15-1	54	-	26	17	-	3	-	-	-	1.28
P 15 4	32	6	37	12	-	2	11	-	-	0.94
JM 1	61	-	25	12	-	2	-	-	-	1.02
JM 2	32	-	8	6	-	-	54	-	-	0.52

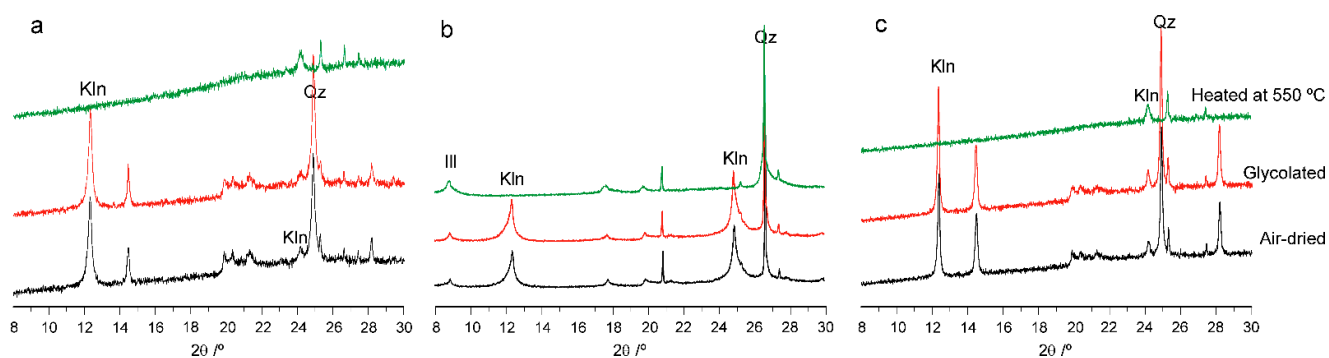


**Figure 3.** Powder XRD patterns of oriented aggregates: (a) sample P1, (b) sample P2, and (c) sample JM1. Kln: Kaolinite group; Ill: Illite; Qz: Quartz.

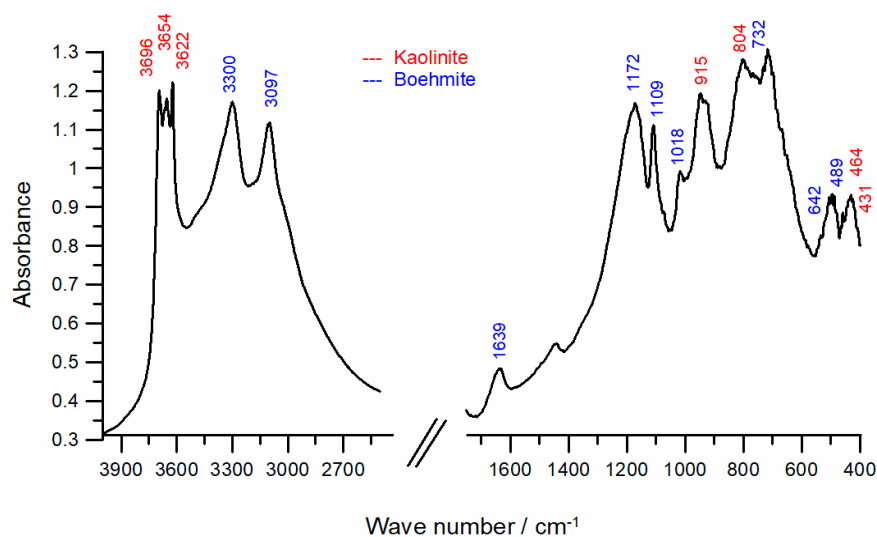
Kaolinite has been observed in SEM as regular hexagonal flakes, 1 to 10  $\mu\text{m}$  in size, sometimes found in stacks. Besides its morphology, the crystallinity of kaolinite has a great influence on its behavior. To assess this parameter, the development of different crystallinity indices has been suggested [35,36]. In the present study, the crystallinity of kaolinite was evaluated by means of the Hinckley crystallinity index, HI (Table 2) [37].

This index depends on the degree of ordering in the kaolinite structure, with values ranging from less than 0.5 in disordered structures to 1.5 in ordered ones [36]. In the studied samples, kaolinite has an HI ranging from 0.51 to 1.39, with lower values corresponding to a lower degree of crystallization.

FTIR spectra confirm the XRD results, with kaolinite and boehmite being the most abundant minerals (Figure 4, Table 3). The characteristic patterns of kaolinite resulted from  $\text{SiO}_4\text{-Al}_2\text{O}_3$  structural bonds (Si-O-Al), octahedral aluminum bonds (Al-O and Al-OH), and tetrahedral silica bonds (Si-O).

**Table 3.** Assignment of FTIR bands (in  $\text{cm}^{-1}$ ) of bauxitic samples from Peramola and Sant Joan de Mediona.

Kaolinite [19]	Boehmite [38,39]	P1	P2-B	P3	JM1	Assignment
3670–3656		3693	3699	3695	3696	Al-OH stretching
3645		3654	3654	3655	3654	Al-OH stretching
3620		3622	3625	3623	3622	Al-OH stretching
	3295	3295		3299	3300	Al-OH stretching
	3090	3103		3104	3097	Al-OH stretching
1638		1638	1639	1638	1639	H-O-H stretching
	1160	1150		1164	1172	H-O-H stretching
1117–1105		1108	1112	1112	1109	Si-O stretching
	1067	1020		1020	1018	H-O-H stretching
		945	950	947	948	Si-O
918–909		919	924	931	915	OH deformation
800–784		821	803	794	804	OH deformation
	730	728		750	732	Si-O-Al stretching
700–686		709	698	730	700	Si-O
	624	640		716	642	Si-O-Al stretching
535–524		556	530	520	523	Si-O-Al stretching
	490	528		489	489	Si-O-Al stretching
475–468		460	479	462	464	Si-O-Si bending
430		426	431	440	431	Si-O Bending

**Figure 4.** FTIR spectrum corresponding to a kaolinite- and boehmite-rich sample (JM1).

The absorption bands related to Al-OH stretching are observed between 3670 and 3622  $\text{cm}^{-1}$ . Si-O stretching bands occur at 1120 and 945  $\text{cm}^{-1}$ . The structure of boehmite consists of a double layer of octahedral oxygen, partially filled with Al cations, detecting Al-OH and H-O-H bonds [38–40]. The intensity of the main boehmite events can vary according to the particle size [41].

### 3.3. Rheological Properties

The Atterberg limits of the studied materials are presented in the Supplementary File. Most of the samples show a correlation between the liquid limit and the plastic limit, except for two cases in which the liquid limit was close to zero. According to the Holtz and Kovacs diagram [42], most of the studied bauxitic materials are low plastic, and locally, they can be medium plastic (Figure 5, Table S1). Particle size distribution and mineralogical composition has significant influence on plasticity, increasing with kaolinite and other clay mineral contents and decreasing the hematite, boehmite, quartz, and calcite contents [43].

The carbonate-rich sample from the Sant Joan de Mediona plot similar to the carbonate-poor sample P3. There is no clear correlation between the clay content and the plasticity of the samples; however, the three samples with medium-to-high plasticity (P14-3, P11-B, and P2) are characterized by a significant illite content and an absence of boehmite (Table 2).

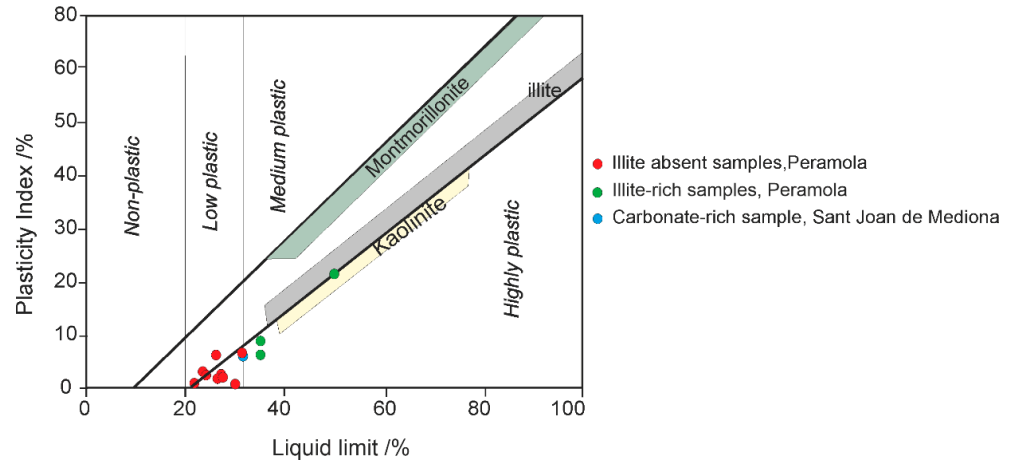


Figure 5. Holtz and Kovacs plasticity diagram [41] of Kaolinitic materials from Peramola and Sant Joan de Mediona. Plastic limits established from [44].

Plasticity is one of the most important parameters in determining the feasibility of manufacturing ceramic products. In the case of materials with low plasticity, they are not suitable for pottery but are suitable for the manufacture of bricks [45]. Low plasticity indices are common in bauxitic materials [46,47]. It was suggested that these materials could act as plasticity reducers to make ceramic materials [48].

3.4. Thermal Evolution

DTA-TG results are summarized in Table 4. All samples show two endothermic peaks in the range 300–1100 °C; the first is attributed to a partial dehydroxylation and transformation of boehmite to  $\gamma\text{-Al}_2\text{O}_3$  [49–52]. The temperature of this endothermic peak is correlated with the size of the crystal [49,52], being at 530 °C in the analyzed samples. The other peak, found near 560 °C, is caused by the loss of structural  $\text{OH}^-$  groups of kaolinite and is related to the maximum weight loss observed in the TG curves.

Table 4. Thermal events measured by DTA-TG during heating from 25 to 1100 °C.

Sample	Temperature/°C				Weight Loss/%			
	Endothermic		Exothermic		Adsorbed Water < 200 °C	Structural Water 400–550 °C	Structural Water > 550 °C	Decarbonization
	1 Boehmite	2 Kaolinite	$\gamma\text{-Al}_2\text{O}_3 \rightarrow \theta\text{-Al}_2\text{O}_3$	Mullite Formation				
P1	538	568	-	978	0.55	5	6	-
P2	-	547	-	950	1.89	4	4	-
P3	530	568	952	972	1.49	6	5	-
P10-B	530	547	954	970	2.66	9	7	-
JM 1	536	564	-	966	0.37	6	5	-
JM 2	-	535	953	-	1.7	6	-	17

During heating, the  $\gamma\text{-Al}_2\text{O}_3$  is transformed to  $\delta\text{-Al}_2\text{O}_3$ , which changes to  $\theta\text{-Al}_2\text{O}_3$ , and this to the more-stable-phase  $\alpha\text{-Al}_2\text{O}_3$ . The boehmite-richest samples show a weak exothermic peak at 952–954 °C, which is probably associated with the transition from  $\gamma\text{-Al}_2\text{O}_3$  to  $\theta\text{-Al}_2\text{O}_3$  [52]. The transformation  $\theta\text{-Al}_2\text{O}_3$  to  $\alpha\text{-Al}_2\text{O}_3$  occurs at temperatures above 1000 °C [49,52] and was not observed in the DTA analyses of the studied samples, which

were treated at more than 1100 °C. This transition usually occurs above 1100 °C [49–54]; however, it has been reported that in some cases, it starts earlier at 900 °C [53]. Therefore, it cannot be ruled out that the small exotherm observed around 950 °C corresponds to the transformation to  $\alpha$ -Al<sub>2</sub>O<sub>3</sub>. In the samples studied, the temperature at which this transformation occurs could be affected by the influence of the other components.

A sharp exothermic peak occurs between 950 and 978 °C due to the transformation of metakaolinite and alumina into mullite [55] (Figure 6). The carbonate-rich samples show an endothermic event related to the decarbonation reaction, in which calcite (CaCO<sub>3</sub>) decomposes into CaO and CO<sub>2</sub>, which correlates to a significant weight loss (17 wt%).

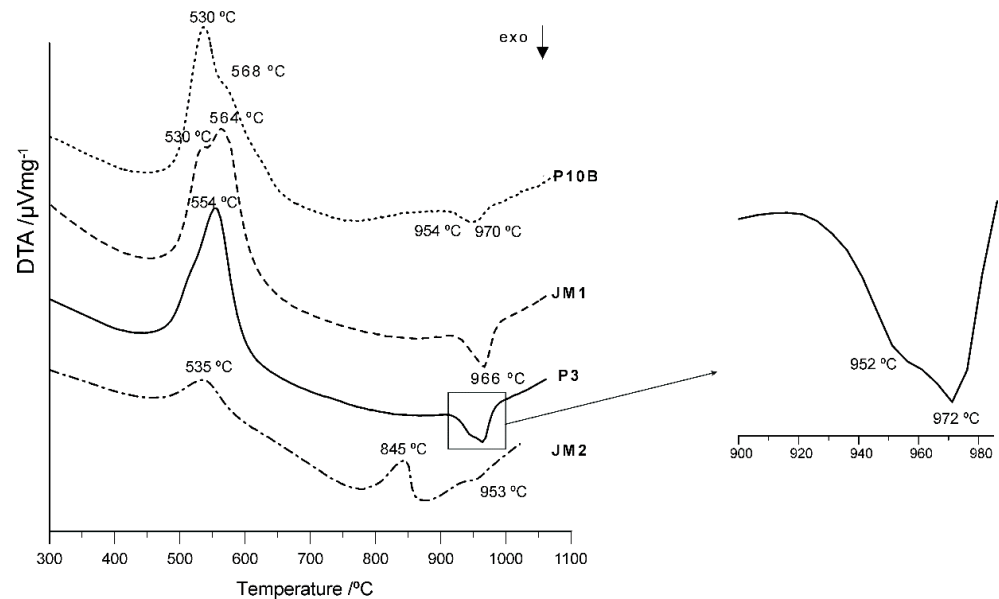


**Figure 6.** DTA curves of boehmite-rich samples (P10B and P3), carbonate and quartz-poor sample (JM1), and a carbonate-rich sample (JM2).

The mass loss at temperatures below 200 corresponds to the adsorption water of the sample, which requires the least energy to remove from the structure and is therefore easily lost. The loss between 400 and below 540 °C is associated with structural hydroxyl groups in boehmite. Tsukada et al. [53] suggested that boehmite contains two types of hydroxy groups, one of which dehydrates during the conversion of boehmite to  $\gamma$ -Al<sub>2</sub>O<sub>3</sub>, corresponding to weight losses around 530 °C; and the other group remains linked to  $\gamma$ -Al<sub>2</sub>O<sub>3</sub>, which gradually being lost with heating. This results in weight losses of up to 7%. The weight loss around 550 °C is related to structural changes in kaolinite.

### 3.5. Technological Properties

A comparison of the technological properties was made according to the most relevant mineralogical characteristics of the studied materials. All samples contain kaolinite. However, among them, a distinction was made between samples rich in quartz and illite (P2, P11-B, P14-3), samples rich in carbonate (JM2, P14-1), and samples poor in quartz and carbonates. The differentiation of samples with illite was based on their higher plasticity. The specific contemplation of materials with carbonates was based on the fact that these minerals contribute a large amount of calcium to the system, which causes a great difference in the possible phases generated during firing [56]. Samples P2, JM2, and P3 were used for the gresification tests.

#### 3.5.1. Gresification Curves

Linear firing shrinkage and water absorption has an inverse correlation, as linear cooking shrinkage occurs when both chemically and mechanically bound water is released [57]. Materials from Peramola and Sant Joan de Mediona show variable behavior with regard

to shrinkage during their heating. In all cases, shrinkage occurs when subjected to high temperature; the absorbance of water decreases (Figure 7).

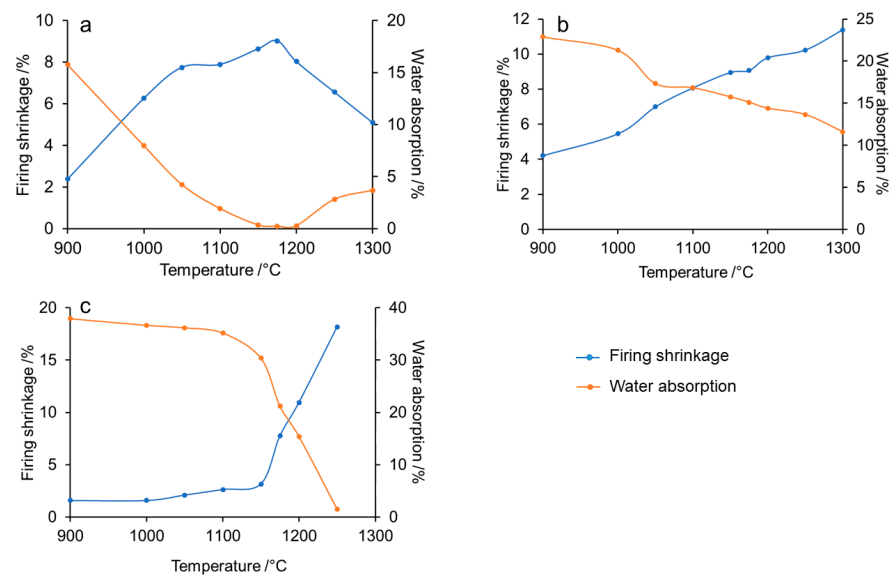


**Figure 7.** Gresification curves of fired representative samples: (a,b) Peramola (P 2 and P 3); and (c), Sant Joan de Mediona (JM 2).

In quartz-rich materials, this increase reaches a maximum, around 1150–1200 °C, and from this temperature, an expansion occurs. In this case, the water absorption is minimal at the temperature of maximum shrinkage, even reaching zero (Figure 7a), implying that a ceramic material fired to these temperatures will be waterproof. As the samples expand again during heating, the water absorption also increases, i.e., a blind porosity has occurred. (Figure 7a). The decrease in water absorption can also be predicted from the observation of SEM images where intergranular porosity decreases at high temperatures (Figure 8).

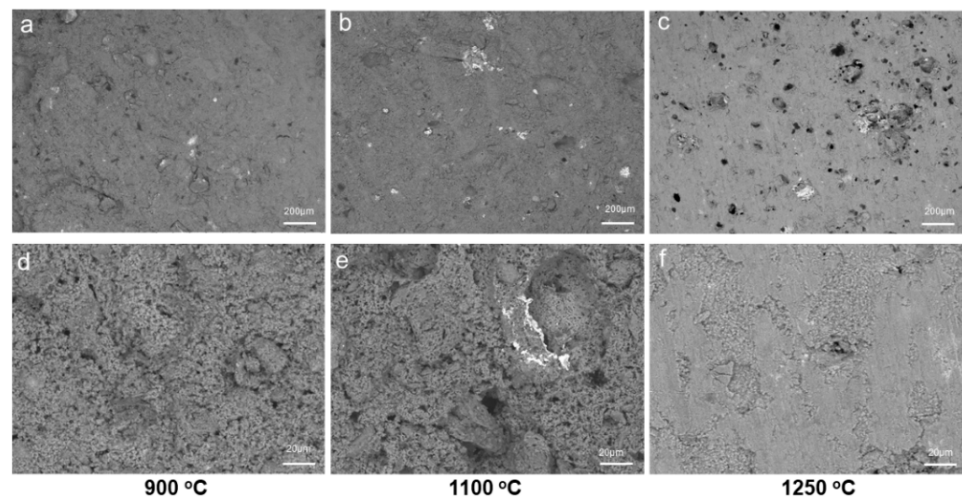


**Figure 8.** SEM images of fired tiles showing intergranular porosity progression with temperature in carbonate-rich materials (JM2): (a,d) sample fired at 900 °C; (b,e) sample fired at 900 °C; (c,f) sample fired at 900 °C.

In other cases, the expansion continues up to temperatures above 1300 °C (Figure 7b). In the case of carbonate-rich samples, the expansion shows two trends, up to about 1150 °C, it increases smoothly, and, from this temperature, it undergoes an abrupt contraction.

In carbonate-rich materials (Figure 7c), lineal shrinkage increases and water absorption decreases slowly until around 1150 °C, and, from this temperature, linear shrinkage

increases more rapidly during heating, and water absorption decreases more sharply. This can be attributed to the reaction of the lime formed from the calcination of calcite and metakaolinite formed by the dehydroxylation of kaolinite to form a liquid phase, which rapidly decreases with increasing firing temperature forming crystalline phases [58]. Similar effects of carbonates have been observed when coexisting with other types of clays, such as illite [59].

Sintering temperatures can be determined from the intersection between the firing shrinkage and the water absorption curves. In the analyzed materials, the optimal sintering temperatures are near 970 °C for carbonate-poor, illite-rich clays; 1100 °C for quartz, carbonate-poor materials; and near 1190 °C for carbonate-rich materials (Figure 7).

The shrinkage produced during firing is a consequence of the reduction in porosity developed as a consequence of the loss of intergranular porosity caused by the formation of a glassy phase from the destruction of metakaolinite and the later crystallization of new phases [31,60,61]. In SEM observations, tiles fired at 1250 °C show textures indicative of sinterization having been achieved.

### 3.5.2. Mineralogy of the Fired Materials

The mineralogy of the heated materials, once they have reached stability, can be predicted from the stability diagrams. According to the CaO-SiO<sub>2</sub>-Al<sub>2</sub>O<sub>3</sub> diagram [62], in most of the treated materials, the main component will be mullite. In the case of raw materials with high carbonate content, gehlenite will be formed instead of mullite (Figure 9).

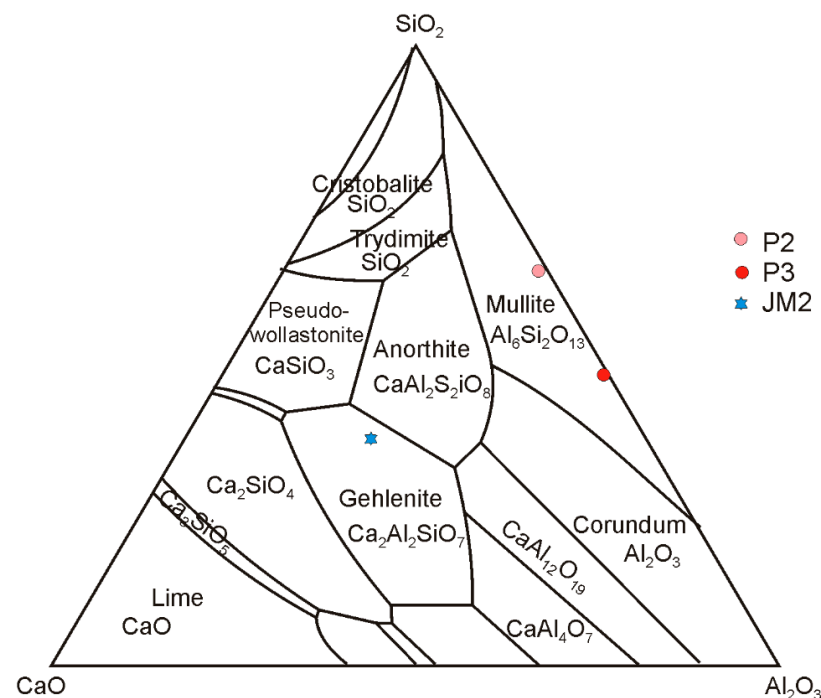


**Figure 9.** CaO-SiO<sub>2</sub>-Al<sub>2</sub>O<sub>3</sub> diagram [62] showing the stability field of the samples from Peramola and Sant Joan de Mediona.

Transformations in mineralogy during heat treatment vary according to the initial mineralogical composition (Figures 10 and 11). In cases of quartz-rich materials, where the Ca content is very low, at 900 °C, metakaolinite occurs as an amorphous phase and quartz is the major crystalline phase, coexisting with moderate amounts of hematite and small amounts of anatase. Although the content of the amorphous phase has not been calculated, its existence and magnitude can be appreciated from the results of the semi-quantitative determination of the quartz content from XRD; for example, sample P2 contained 50% quartz, whereas in the sample heated to 900 °C, the content of this crystalline phase is 87%, indicating at least 43% of amorphous phase.

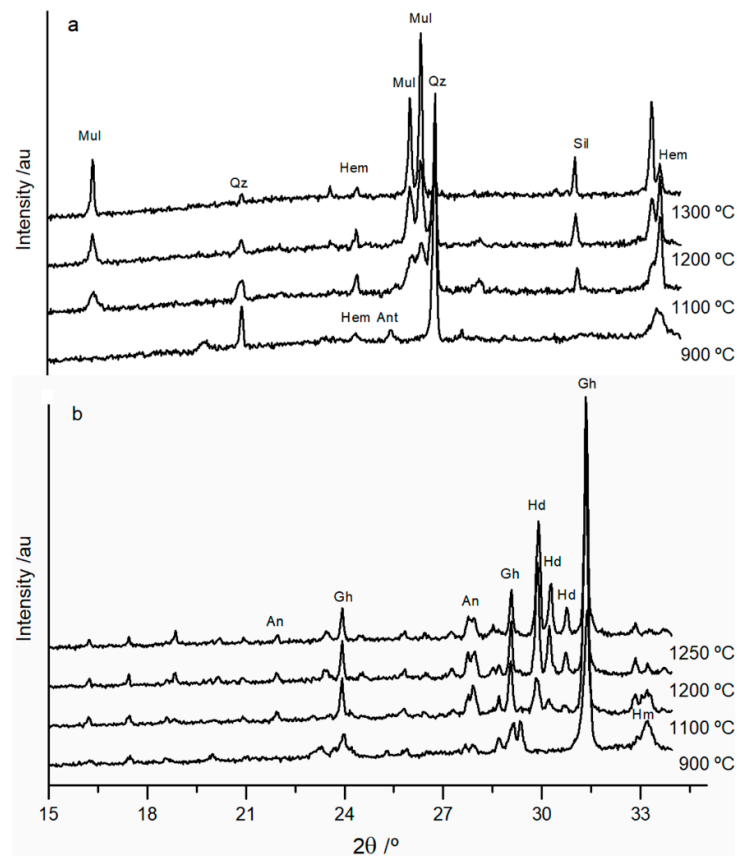


**Figure 10.** XRD patterns for fired materials: (a) tiles from quartz-rich raw materials (sample JM2); (b) tiles from carbonate-rich raw materials (sample P2). Mul: mullite; Qz: quartz; Hm: hematite; Ant: anatase; Sil: sillimanite; An: anorthite; Gh: gehlenite; Hd: hedenbergite.

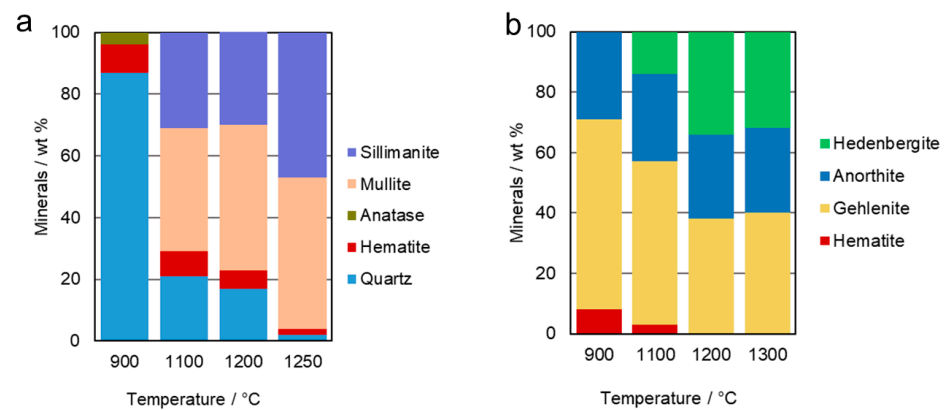


**Figure 11.** Crystalline phases of the fired materials: (a) tiles from quartz-rich raw materials (sample P2); (b) tiles from carbonate-rich raw materials (sample JM2).

At 1100 °C, the quartz content has decreased drastically, transforming into an amorphous phase and contributing to the formation of the sillimanite ( $\text{Al}_2\text{SiO}_5$ ) and mullite ( $\text{Al}_6\text{Si}_2\text{O}_{13}$ ) (Figure 12a–d). Sillimanite and mullite have similar morphological and structural characteristics, but mullite is stable at higher temperatures, with the mullitization limit being established at 932 °C, i.e., when  $\text{Al}_2\text{O}_3$  predominates over  $\text{SiO}_2$  [63,64].

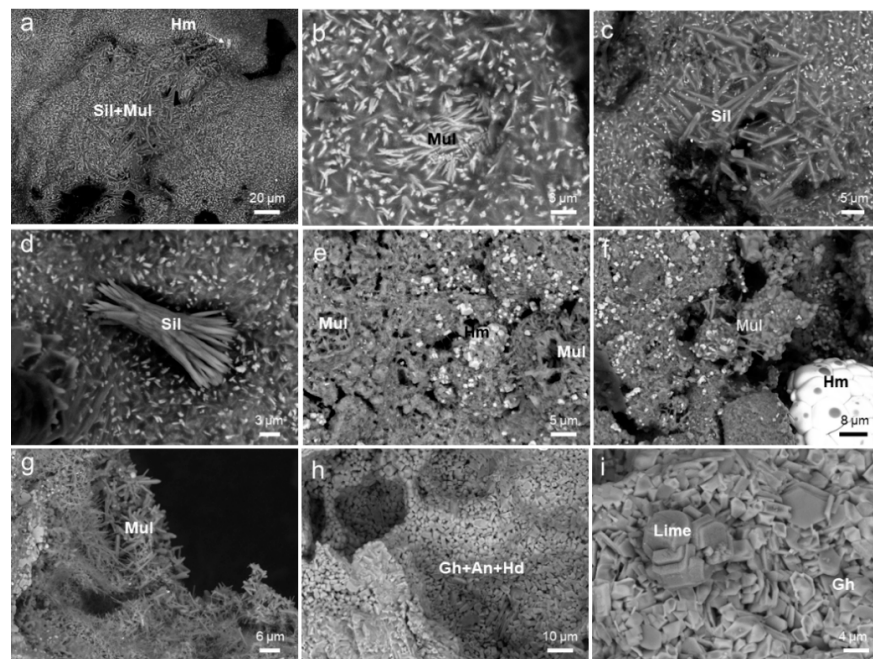


**Figure 12.** SEM images of fired materials: (a–d) Tiles from quartz-rich raw materials; (e–g) tiles from quartz, carbonate-poor materials (h,i); tiles from carbonate-rich raw materials. Sil: sillimanite; Mul: mullite; Hm: hematite; Gh: gehlenite; An: anorthite; hd: hedenbergite.

In the fired materials analyzed in this study, the presence of cristobalite has not been detected. The occurrence of cristobalite occurs from 1300 °C onwards [65].

During heating, there is a significant reduction in the hematite content. Part of the  $\text{Fe}^{3+}$  from the hematite could have been located in replacing the position of Al in the structure of Mullite, and some of the  $\text{Fe}^{3+}$  could have been in the amorphous phase [66]. When the raw material contains very high amounts of hematite, the hematite remains in the treated samples even at 1300 °C, e.g., in sample P3 (Figure 12e–g).

In the case of carbonate-rich sample JM2, as kaolin and calcite decompose, in addition to  $\text{SiO}_2$  and  $\text{Al}_2\text{O}_3$ , calcium is available, which favors the formation, initially, of gehlenite and anorthite (Figure 12h). Hematite occurs up to 1200 °C; then, it decomposes, and liberated  $\text{Fe}^{3+}$  is reduced. From this temperature onwards, the availability of  $\text{Fe}^{2+}$  favors the formation of hedenbergite from gehlenite. High Ca contents prevent the formation of mullite in favor of calcium-rich crystalline phases [67].

In the sintering process of carbonate-rich samples, the presence of crystals of CaO was observed (Figure 12i). Their formation is due to the fact that some calcite grains that have not been ground properly during grinding act as a degreaser, or non-plastic component, in the ceramic paste. These grains are more resistant during the firing process of the body. The free lime formed when the decarbonation of the carbonates begins at 900 °C interacts on its surface with the silica and alumina from the decomposition of the clay, giving rise to gehlenite and anorthite. When the calcite grain size is larger, not all the CaO is fully reacted during firing, which occurs layer by layer. Its formation can become a problem later on for the fired ceramic piece as, over time, it can react with water and form lime hydroxide; the expansion due to this reaction can cause the ceramic piece to break at specific points.



### 3.5.3. Color of Fired Tiles

The color of raw materials can change significantly during heat treatment at elevated temperatures. The color of the tiles principally depends on  $\text{Fe}_2\text{O}_3$  and  $\text{TiO}_2$  content, but the

mineralogy also has an influence. Moreover, K, Na, and Mg affect the brick color. The Na and Mg content is negligible in the studied material. K is significant in illite-rich samples. In this case, during firing, K probably migrated to the amorphous phase [68]. The bauxitic clays have a reddish color, and in all cases, the tiles became darker with the firing. This change was attributed to the change of their mineralogical composition [68].

In the initial stages, color is conditioned by the amount of hematite. In all cases after a certain temperature, there is a reduction of  $a^*$  and  $b^*$  parameters (Figure 13). This reduction is related to the amount of free hematite present in the sample [69]. In quartz-rich samples, the increase in the  $a^*$  chromatic coordinate after 1200 °C due to the destruction of illite structure, where  $\text{Fe}^{3+}$  is liberated, forms new phases or crystallize into hematite, increasing the reddish color (Figure 13) [70,71]. The decrease in the  $a^*$  coordinate can be associated with the formation of mullite, which can absorb part of hematite, leading to whiter colors. In both fired materials, Peramola and Sant Joan de Mediona, the  $C^*$  coordinate decreases with temperature increase due to formation of iron and/or titanium oxides. The carbonate-rich materials initially show a reddish color due to the presence of hematite, but later, when hematite is destroyed and Fe is reduced, the  $C^*$  and  $b^*$  coordinates increase, giving a whiter color to the sample until near 1150 °C. After this temperature, these coordinates decrease again.

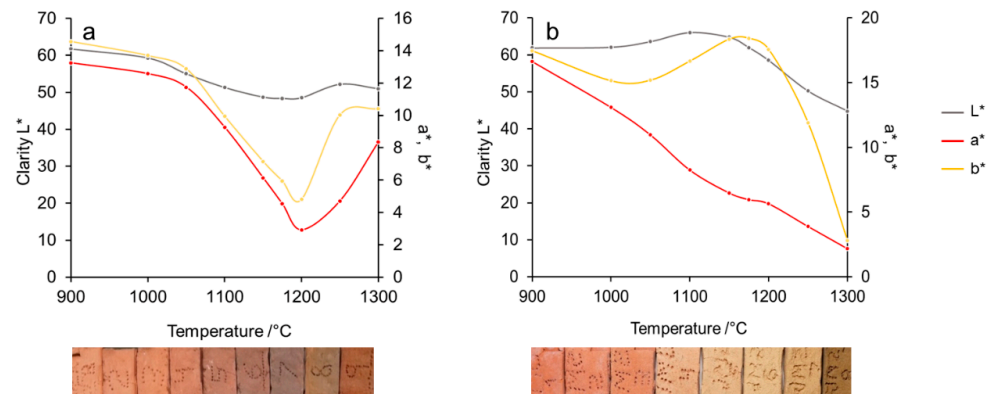


**Figure 13.** Color coordinates through different temperatures and their visible color: (a) quartz-rich sample, P2; (b) carbonate-rich sample, JM2.

#### 4. Conclusions

Bauxitic materials from Sant Joan de Mediona and Peramola contain a significant amount of kaolinite, which is accompanied by boehmite, iron oxides, and minor rutile and anatase. Non-homogeneously distributed, they may contain calcite and quartz and illite.

The bauxitic materials had low plasticity, except those rich in illite, which had medium-to-high plasticity.

The curves obtained by plotting the evolution of liner shrinkage and water absorption with temperature show an inverse correlation. From the intersection of these curves, the optimum firing temperature for obtaining the ceramic product was determined. The illite-rich samples showed the lowest firing temperature (970 °C), those poor in illite and carbonate sintered at 1100 °C, and the carbonate-rich samples presented the highest firing temperature (around 1190 °C).

The mineralogy of the fired products varies according to the carbonate content: mullite and sillimanite are formed in poor-calcite materials; while gehlenite, anorthite, and hedenbergite crystallize in carbonate-rich ones. Therefore, the presence of carbonate levels intercalated in these materials at the time of stockpiling must be considered in future use, since they will cause a change in the mineralogy. From all these minerals, resistant ceramic products result. However, the plasticity of these materials is usually low.

Most of the bauxitic materials studied could be used in the formulation of ceramic pastes for the manufacture of bricks or tiles due to their low plasticity. Additionally, their high  $\text{Al}_2\text{O}_3$  contents made them suitable for use as parts of blends contributing to the

production of refractory ceramics. They could also be used in the formulation of the paste as plasticity reducers. The illite-rich materials could be used for stoneware but are present in reduced content. On the other hand, the color of all these materials is dark red, which also limits their possible applications.

**Supplementary Materials:** The following supporting information can be downloaded at: <https://www.mdpi.com/article/10.3390/min13101294/s1>. Table S1: rheological properties of the studied materials.

**Author Contributions:** Conceptualization, P.A. and M.G.-V.; methodology, M.G.-V. and P.A.; Field work: A.M., M.G.-V. and P.A.; software, P.A. and M.G.-V.; validation, P.A. and M.G.-V.; formal analysis, M.G.-V. and A.M.; investigation, A.M., M.G.-V. and P.A.; data curation, A.M.; writing—original draft preparation, A.M., P.A. and M.G.-V.; writing—review and editing, A.M., P.A. and M.G.-V.; supervision, P.A. and M.G.-V.; project administration, M.G.-V. and P.A.; funding acquisition, M.G.-V. and P.A. All authors have read and agreed to the published version of the manuscript.

**Funding:** This research was partially funded by the Generalitat de Catalunya (Autonomous Government of Catalonia) to the Consolidated Research Groups SGR 01041 (RIIS) and SGR 00262 (GEOXiS).

**Data Availability Statement:** Not applicable.

**Acknowledgments:** We are grateful for the extensive comments of two anonymous reviewers, who helped to improve the manuscript, and to the editors of *Minerals*.

**Conflicts of Interest:** The authors declare no conflict of interest.

## References

1. Murray, H.H. Traditional and new applications for kaolin, smectite, and palygorskite: A general overview. *Appl. Clay Sci.* **2000**, *17*, 207–221. [[CrossRef](#)]
2. Liew, Y.M.; Kamarudin, H.; Al Bakri, A.M.; Luqman, M.; Nizar, I.K.; Heah, C.Y. Investigating the possibility of utilization of kaolin and the potential of metakaolin to produce green cement for construction purposes—A review. *Aust. J. Basic Appl. Sci.* **2011**, *5*, 441–449.
3. Cardinaud, G.; Rozière, E.; Martinage, O.; Loukili, A.; Barnes-Davin, L.; Paris, M.; Deneele, D. Calcined clay–Limestone cements: Hydration processes with high and low-grade kaolinite clays. *Constr. Build. Mater.* **2021**, *277*, 122271. [[CrossRef](#)]
4. da Silva, M.R.C.; Malacarne, C.S.; Longhi, M.A.; Kirchheim, A.P. Valorization of kaolin mining waste from the Amazon region (Brazil) for the low-carbon cement production. *Case Stud. Constr. Mater.* **2021**, *15*, e00756. [[CrossRef](#)]
5. Zheng, S.; Zhou, X.; Xing, W.; Zhao, P. Analysis on the evolution characteristics of kaolin international trade pattern based on complex networks. *Resour. Policy* **2022**, *77*, 102783. [[CrossRef](#)]
6. Barreto, I.A.R.; da Costa, M.L. Use of the clayey cover of bauxite deposits of the Amazon region for geopolymer synthesis and its application in red ceramics. *Constr. Build. Mater.* **2021**, *300*, 124318. [[CrossRef](#)]
7. Melo, C.C.A.; Melo, B.L.S.; Angelica, R.S.; Paz, S.P.A. Gibbsite-kaolinite waste from bauxite beneficiation to obtain FAU zeolite: Synthesis optimization using a factorial design of experiments and response surface methodology. *Appl. Clay Sci.* **2019**, *170*, 125–134. [[CrossRef](#)]
8. Sglavo, V.M.; Maurina, S.; Conci, A.; Salviati, A.; Carturan, G.; Cocco, G. Bauxite red mud in the ceramic industry. Part 2: Production of clay-based ceramics. *J. Eur. Ceram. Soc.* **2000**, *20*, 245–252. [[CrossRef](#)]
9. Yalçın, N.; Sevinç, V. Utilization of bauxite waste in ceramic glazes. *Ceram. Int.* **2000**, *26*, 485–493. [[CrossRef](#)]
10. Dong, Y.; Feng, X.; Ding, Y.; Liu, X.; Meng, G. Preparation of low-cost mullite ceramics from natural bauxite and industrial waste fly ash. *J. Alloys Compd.* **2008**, *460*, 599–606. [[CrossRef](#)]
11. Fernández-Caliani, J.C.; Galán, E.; Aparicio, P.; Miras, A.; Márquez, M.G. Origin and geochemical evolution of the Nuevo Montecastelo kaolin deposit (Galicia, NW Spain). *Appl. Clay Sci.* **2010**, *49*, 91–97. [[CrossRef](#)]
12. Martín-Moreno, C.; Martín-Duque, J.F.; Nicolau, J.M.; Sanchez, L.; Ruiz, R.; Sanz, M.A.; Lucía, A.; Zapico, I. A geomorphic approach for the ecological restoration of kaolin mines at the Upper Tagus Natural Park (Spain). In Proceedings of the 6th European Conference on Ecological Restoration, Ghent, Belgium, 8–12 September 2008; pp. 8–12.
13. Dondi, M.; García-Ten, J.; Rambaldi, E.; Zanelli, C.; Vicent-Cabedo, M. Resource efficiency versus market trends in the ceramic tile industry: Effect on the supply chain in Italy and Spain. *Resour. Conserv. Recycl.* **2021**, *168*, 105271. [[CrossRef](#)]
14. Molina, J.M. Paleokarsts in Spain. *Acta Geol. Hung.* **1991**, *34*, 179–194.
15. Salas, R.; Vaquer, R.; Travé, A. Bauxitas kársticas y arcillas lateríticas barremienses de la Cadena Ibérica oriental y la Cadena Costera Catalana: Relaciones genéticas y áreas de procedencia. *Geotemas* **2004**, *6*, 123–126.
16. Yuste, A.; Bauluz, B.; Mayayo, M.J. Genesis and mineral transformations in Lower Cretaceous karst bauxites (NE Spain): Climatic influence and superimposed processes. *Geol. J.* **2015**, *50*, 839–857. [[CrossRef](#)]

17. Yuste, A.; Bauluz, B.; Mayayo, M.J. Origin and geochemical evolution from ferrallitized clays to karst bauxite: An example from the Lower Cretaceous of NE Spain. *Ore Geol. Rev.* **2017**, *84*, 67–79. [[CrossRef](#)]
18. Reinhardt, N.; Proenza, J.A.; Villanova-de-Benavent, C.; Aiglsperger, T.; Bover-Arnal, T.; Torró, L.; Salas, R.; Dziggel, A. Geochemistry and mineralogy of rare earth elements (REE) in Bauxitic ores of the Catalan Coastal Range, NE Spain. *Minerals* **2018**, *8*, 562. [[CrossRef](#)]
19. Garcia-Valles, M.; Alfonso, P.; Martínez, S.; Roca, N. Mineralogical and thermal characterization of kaolinitic clays from Terra Alta (Catalonia, Spain). *Minerals* **2020**, *10*, 142. [[CrossRef](#)]
20. Vergés, J.; Munoz, J.A. Thrust sequence in the southern central Pyrenees. *Bull. Soc. Géol. Fr. BSGF* **1990**, *6*, 265–271. [[CrossRef](#)]
21. Burbank, D.W.; Verges, J.; Muñoz, J.A.; Bentham, P. Coeval hindward-and forward-imbricating thrusting in the south-central Pyrenees, Spain: Timing and rates of shortening and deposition. *Geol. Soc. Am. Bull.* **1992**, *104*, 3–17. [[CrossRef](#)]
22. Molina, J.M.; Ruiz-Ortiz, P.A.; Vera, J.A.; Calonge, A. Bauxitas kársticas de la Sierra de Boada. *Geogaceta* **1994**, *16*, 148–150.
23. Closas i Miralles, J. Els nous jaciments de bauxita. *Bulletí Inst. Catalana D'història Nat.* **1949**, 22–29.
24. Closas i Miralles, J. Las bauxitas del NE de España. *XIX Congr. Geol. Intern* **1952**, *12*, 199–223.
25. Moore, D.M.; Reynolds, R.C., Jr. *X-ray Diffraction and The Identification and Analysis of Clay Minerals*, 2nd ed.; Oxford University Press OUP: Oxford, UK, 1997.
26. Plançon, A.; Giese, R.F.; Snyder, R. The Hinckley index for kaolinites. *Clay Miner.* **1988**, *23*, 249–260. [[CrossRef](#)]
27. AENOR. *UNE 7-377-75*; Determinación del Límite Líquido de un Suelo por el Método de la Cuchara. UNE: Madrid, Spain, 1976.
28. AENOR. *UNE 103-104-93*; Determinación del Límite Plástico de un Suelo. UNE: Madrid, Spain, 1993.
29. *UNE-EN ISO 10545-3:2018*; Ceramic Tiles—Part 3: Determination of Water Absorption, Apparent Porosity, Apparent Relative Density and Bulk Density (ISO 10545-3:2018). ISO: Madrid, Spain, 2018.
30. Baccour, H.; Medhioub, M.; Jamoussi, F.; Mhiri, T. Influence of Firing Temperature on the Ceramic Properties of Triassic Clays from Tunisia. *J. Mater. Proc. Technol.* **2009**, *209*, 2812–2828. [[CrossRef](#)]
31. Garcia-Valles, M.; Cuevas, D.; Alfonso, P.; Martínez, S. Thermal behaviour of ceramics obtained from the kaolinitic clays of Terra Alta, Catalonia, Spain. *J. Thermal Anal. Calorim.* **2022**, *147*, 5303–5312. [[CrossRef](#)]
32. CIELab CIE. *Technical Report, Colorimetry*; Commission Internationale de L'Eclairage: St. Paul, MN, USA, 1931.
33. Bárdossy, G.; Aleva, G.J.J. *Lateritic Bauxites: Developments in Economic Geology*; Elsevier Science: Amsterdam, The Netherlands, 1990; 624p.
34. Laita, E.; Bauluz, B.; Mayayo, M.J.; Yuste, A. Mineral and textural transformations in mixtures of Al-rich and Al-K-rich clays with firing: Refractory potential of the fired products. *Ceram. Int.* **2021**, *47*, 14527–14539. [[CrossRef](#)]
35. Galán, E.; Aparicio, P.; Gonzalez, I.; Miras, A. Contribution of multivariate analysis to the correlation of some properties of kaolin with its mineralogical and chemical composition. *Clay Miner.* **1998**, *33*, 65–75. [[CrossRef](#)]
36. Aparicio, P.; Galán, E. Mineralogical interference on kaolinite crystallinity index measurements. *Clays Clay Miner.* **1999**, *47*, 12–27. [[CrossRef](#)]
37. Hinckley, D.N. Mineralogical and chemical variations in kaolin deposits of the coastal plain of Georgia and South Carolina. *Am. Miner.* **1965**, *70*, 1865–1883.
38. Christoph, G.G.; Corbato, C.E.; Hofmann, D.A.; Tettenhorst, R.T. The crystal structure of boehmite. *Clays Clay Miner.* **1979**, *27*, 81–86. [[CrossRef](#)]
39. Klopogge, J.T.; Ruan, H.D.; Frost, R.L. Thermal decomposition of bauxite minerals: Infrared emission spectroscopy of gibbsite, boehmite and diaspore. *J. Mater. Sci.* **2002**, *37*, 1121–1129. [[CrossRef](#)]
40. Balde, M.Y.; Djangang, C.N.; Diallo, R.B.; Blanchart, P.; Njopwouo, D. Physicochemical Characterisation for Potential Uses as Industrial Mineral of Bauxite from Débélé, Guinea. *J. Mater. Sci. Chem. Eng.* **2021**, *9*, 9–22.
41. Tettenhorst, R.; Hofmann, D.A. Crystal chemistry of boehmite. *Clays Clay Miner.* **1980**, *28*, 373–380. [[CrossRef](#)]
42. Holtz, R.D.; Kovacs, W.D. *An Introduction to Geotechnical Engineering*, 1st ed.; Prentice-Hall: Englewood Cliffs, NJ, USA, 1981; 733p.
43. El Ouahabi, M.; Daoudi, L.; Fagel, N. Mineralogical and geotechnical characterization of clays from northern Morocco for their potential use in the ceramic industry. *Clay Miner.* **2014**, *49*, 35–51. [[CrossRef](#)]
44. Salah, I.B.; Sdiri, A.; Jemaia, M.B.M.; Boughdiria, I.M. Potential use of the lower Cretaceous clay (Kef area, Northwestern Tunisia) as raw material to supply ceramic industry. *Appl. Clay Sci.* **2018**, *161*, 151–162. [[CrossRef](#)]
45. Kagonbé, B.P.; Tsozué, D.; Nzeukou, A.N.; Ngos, S., III. Mineralogical, physico-chemical and ceramic properties of clay materials from Sekandé and Gashiga (North, Cameroon) and their suitability in earthenware production. *Heliyon* **2021**, *7*, e07608. [[CrossRef](#)]
46. Dodoo-Arhin, D.; Konadu, D.S.; Annan, E.; Buabeng, F.P.; Yaya, A.; Agyei-Tuffour, B. Fabrication and characterisation of Ghanaian bauxite red mud-clay composite bricks for construction applications. *Am. J. Mater. Sci.* **2013**, *3*, 110–119.
47. Mishra, M.C.; Reddy, N.G.; Rao, B.H. Potential of citric acid for treatment of extremely alkaline bauxite residue: Effect on geotechnical and geoenvironmental properties. *J. Hazard. Toxic Radioact. Waste* **2020**, *24*, 04020047. [[CrossRef](#)]
48. de Azevedo, A.R.G.; Marvila, M.T.; de Oliveira, M.A.B.; Umbuzeiro, C.E.M.; Huaman, N.R.C.; Monteiro, S.N. Perspectives for the application of bauxite wastes in the development of alternative building materials. *J. Mater. Res. Technol.* **2022**, *20*, 3114–3125. [[CrossRef](#)]
49. Bokhimi, X.; Toledo-Antonio, J.A.; Guzman-Castillo, M.L.; Mar-Mar, B.; Hernandez-Beltran, F.; Navarrete, J. Dependence of boehmite thermal evolution on its atom bond lengths and crystallite size. *J. Solid State Chem.* **2001**, *161*, 319–326. [[CrossRef](#)]

50. Denigres Filho, R.W.N.; Rocha, G.D.A.; Montes, C.R.; Vieira-Coelho, A.C. Synthesis and characterization of boehmites obtained from gibbsite in presence of different environments. *Mater. Res.* **2016**, *19*, 659–668. [[CrossRef](#)]
51. Frost, R.L.; Vassallo, A.M. The dehydroxylation of the kaolinite clay minerals using infrared emission spectroscopy. *Clays Clay Miner.* **1996**, *44*, 635–651. [[CrossRef](#)]
52. Földvári, M. *Handbook of Thermogravimetric System of Minerals and Its Use in Geological Practice*; Geological Institute of Hungary: Budapest, Hungary, 2011; Volume 213.
53. Tsukada, T.; Segawa, H.; Yasumori, A.; Okada, K. Crystallinity of boehmite and its effect on the phase transition temperature of alumina. *J. Mater. Chem.* **1999**, *9*, 549–553. [[CrossRef](#)]
54. Rudolph, M.; Salomon, A.; Schmidt, A.; Motylenko, M.; Zienert, T.; Stöcker, H.; Himcinschi, C.; Amirkhanyan, L.; Kortus, J.; Aneziris, C.G.; et al. Thermally induced formation of transition aluminas from boehmite. *Adv. Engin. Mater.* **2017**, *19*, 1700141. [[CrossRef](#)]
55. Ramachandran, V.S.; Paroli, R.M.; Beaudoin, J.J.; Delgado, A.H. *Handbook of Thermal Analysis of Construction Materials*; William Andrew: Norwich, NY, USA, 2002.
56. Cultrone, G.; Rodriguez-Navarro, C.; Sebastian, E.; Cazalla, O.; De La Torre, M.J. Carbonate and silicate phase reactions during ceramic firing. *Eur. J. Mineral.* **2001**, *13*, 621–634. [[CrossRef](#)]
57. Karaman, S.; Ersahin, S.; Gunal, H. *Firing Temperature and Firing Time Influence on Mechanical and Physical Properties of Clay Bricks*; CSIR: Pretoria, South Africa, 2006.
58. Sousa, S.; Holanda, J. Development of red wall tiles by the dry process using Brazilian raw materials. *Ceram. Int.* **2005**, *31*, 215–222. [[CrossRef](#)]
59. Carretero, M.I.; Dondi, M.; Fabbri, B.; Raimondo, M. The influence of shaping and firing technology on ceramic properties of calcareous and non-calcareous illitic–chloritic clays. *Appl. Clay Sci.* **2002**, *20*, 301–306. [[CrossRef](#)]
60. Celik, H. Technological characterization and comparison of two ceramic clays used for manufacturing of traditional ceramic products in Turkey. *Sci. Min. J.* **2017**, *56*, 137–147.
61. Darbari, Z.; Jaradat, K.A.; Abdelaziz, S.L. Heating–freezing effects on the pore size distribution of a kaolinite clay. *Environ. Earth Sci.* **2017**, *76*, 713. [[CrossRef](#)]
62. Osborn, E.F.; Muan, A. Al<sub>2</sub>O<sub>3</sub>–CaO–SiO<sub>2</sub> system revised and redrawn. In *Phase Equilibrium Diagrams of Oxides System*; Hart, L.D., Ed.; American Ceramic Society and the Edward Orton, Jr., Ceramic Foundation: Columbus, OH, USA, 1960.
63. Igami, Y.; Ohi, S.; Miyake, A. Sillimanite–mullite transformation observed in synchrotron X-ray diffraction experiments. *J. Am. Ceram. Soc.* **2017**, *100*, 4928–4937. [[CrossRef](#)]
64. Montoya, N.; Serrano, F.J.; Reventós, M.M.; Amigo, J.M.; Alarcón, J. Effect of TiO<sub>2</sub> on the mullite formation and mechanical properties of alumina porcelain. *J. Eur. Ceram. Soc.* **2010**, *30*, 839–846. [[CrossRef](#)]
65. Xu, X.; Lao, X.; Wu, J.; Zhang, Y.; Xu, X.; Li, K. Microstructural evolution, phase transformation, and variations in physical properties of coal series kaolin powder compact during firing. *Appl. Clay Sci.* **2015**, *115*, 76–86. [[CrossRef](#)]
66. Liu, Z.; Lian, W.; Liu, Y.; Zhu, J.; Xue, C.; Yang, Z.; Lin, X. Phase formation, microstructure development, and mechanical properties of kaolin-based mullite ceramics added with Fe<sub>2</sub>O<sub>3</sub>. *Int. J. Appl. Ceram. Technol.* **2021**, *18*, 1074–1081. [[CrossRef](#)]
67. Pardo, F.; Meseguer, S.; Jordán, M.M.; Sanfeliu, T.; González, I. Firing transformations of Chilean clays for the manufacture of ceramic tile bodies. *Appl. Clay Sci.* **2011**, *51*, 147–150. [[CrossRef](#)]
68. Wang, R.; Xu, S.; Yue, Y.; Wang, X. Thermal behavior of materials in laser-assisted extreme manufacturing: Raman-based novel characterization. *Int. J. Extreme Manuf.* **2020**, *2*, 032004. [[CrossRef](#)]
69. Barba, A.; Beltrán, V.; Felíu, C.; García, F.; Sánchez, E.; Sanz, V. *Materias Primas para la Fabricación de Soportes de Baldosas Cerámicas*; Instituto de Tecnología Cerámica: Castellón, Spain, 1997.
70. Bouzidi, N.; Siham, A.; Concha-Lozano, N.; Gaudon, P.; Janin, G.; Mahtout, L.; Merabet, D. Effect of chemico-mineralogical composition on color of natural and calcined kaolins. *Color Res. Appl.* **2014**, *39*, 499–505. [[CrossRef](#)]
71. De Bonis, A.; Cultrone, G.; Grifa, C.; Langella, A.; Leone, A.P.; Mercurio, M.; Morra, V. Different shades of red: The complexity of mineralogical and physico-chemical factors influencing the colour of ceramics. *Ceram. Int.* **2017**, *43*, 8065–8074. [[CrossRef](#)]

**Disclaimer/Publisher’s Note:** The statements, opinions and data contained in all publications are solely those of the individual author(s) and contributor(s) and not of MDPI and/or the editor(s). MDPI and/or the editor(s) disclaim responsibility for any injury to people or property resulting from any ideas, methods, instructions or products referred to in the content.